Langmuir

ARTICLE

pubs.acs.org/Langmuir

Mechanics of Nanoindentation on a Monolayer of Colloidal Hollow Nanoparticles

Jie Yin,[†,‡,∥] Markus Retsch,[‡,§,∥] Jae-Hwang Lee,[‡,§] Edwin L. Thomas,[‡,§] and Mary C. Boyce*[,†,‡]

[†]Department of Mechanical Engineering, [‡]Institute for Solider Nanotechnologies, and [§]Department of Materials Science and Engineering, Massachusetts Institute of Technology, Cambridge, Massachusetts 02139, United States

Supporting Information

ABSTRACT: We explore the collective mechanical behavior of monolayer assemblies composed of close-packed arrays of hollow silica nanoparticles using a spherical nanoindentor. Seven types of well-defined hollow nanoparticles are studied with their radii ranging from 100 to 300 nm and shell thickness ranging from 14 to 44 nm. Micromechanical models reveal the underlying deformation mechanisms during indentation, where the consecutive contacting of the indentor with an increasing number of nanoparticles results in a nonlinear increase in the indentation force with penetration depth. Each contacted hollow nanoparticle successively locally bends, flattens, and then locally buckles. The effective indentation modulus of the monolayer film, which is obtained by a Hertzian fit to the experimental data, is found to be proportional to the elastic modulus of the nanoparticle shell material and scales exponentially with the ratio of particle shell thickness t to radius R to the power of 2.3. Furthermore, we find that for a constant film density with the same $^{t}/_{R}$ of the constituent nanoparticles, smaller particles with a thinner shell can provide a higher effective indentation modulus, compared to their larger diameter and thicker shell counterparts. This study provides useful insights and guidance for constructing high-performance lightweight nanoparticle films and coatings with potential applications in tailoring stiffness and mechanical energy absorption.

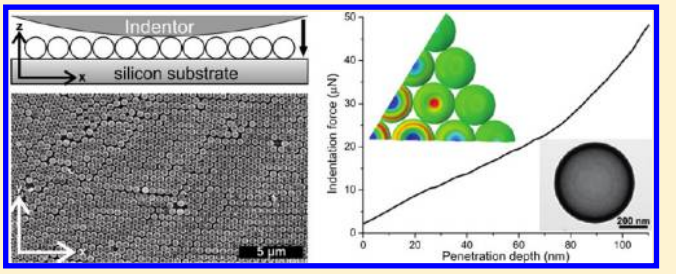

INTRODUCTION

Colloidal hollow nanoparticles (NPs) have become a focal point of study in the fields of medicine, chemistry, and material science for their low density, large surface-to-volume ratio, low refractive index, and controllable shell porosity and cavity volume.[1] With the help of manifold self-assembly techniques,[2−4] dispersed colloidal NPs can self-assemble into a variety of ordered architectures: 2D monolayer arrays,[5−7] 3D multilayer close-packed arrays,[5,8] and 3D colloidal crystals.[9] These hollow NPs and NP arrays have found a wide range of applications in drug/gene delivery,[10] diagnostic imaging,[11] catalysis,[12] photonic band gap materials,[13] nanoelectronics,[14] and magnetic storage.[15] In fulfilling the diverse application functions, the stability and mechanical properties of NPs and NP-based devices are of great importance. Regarding the mechanical properties of individual NPs, Fery and Weinkamer[16] gave a thorough review of the measurement of mechanical properties of individual hollow micro- and nanoparticles under a single-particle compression test. Recently, Zhang et al.[17] studied the elastic properties of single silica NPs by using atomic force microscopy (AFM) and found that the Young's modulus of the silica particle shell is highly related to the annealing temperature.[18] Through the in situ compression of an individual nanocrystalline hollow CdS sphere, Shan et al.[19] found that the hollow NP is capable of withstanding extremely high stress and strain approaching the ideal shear strength of CdS. However, few studies have been conducted on the collective mechanical properties of 2D and 3D NP arrays. Sanders and Gibson[20] conducted a detailed finite element study on the mechanics of hollow sphere foams. Mueggenburg et al.[21] studied the elastic properties of a free-standing 2D composite array composed of a large volume fraction of close-packed solid gold NPs separated by short spacer molecules by using AFM indentation, which revealed the combination of high tensile strength and bending flexibility of the gold nanocrystal monolayers. To the best of our knowledge, the study of the mechanical response and properties of 2D hollow NP arrays remains unexplored. Because of their low density, these hollow NP arrays could find potential applications in constructing lightweight nano/microstructures. They may also be used as efficient energy dissipators upon impact or blast loading.[22]

Here, the mechanical response of a model system, a 2D nanostructured film composed of a monolayer of close-packed hollow silica nanoparticles (HSNP), is investigated during nanoindentation, which allows for a detailed assessment of the individual contributions of particle geometry and material properties with respect to the overall film response. Finite element analysis alongside analytical models is employed to model the experimental results. Our approach follows two lines. First, the nonlinear indentation force−displacement curves are analyzed by

Received: May 13, 2011
Revised: June 27, 2011
Published: June 29, 2011

the Hertzian contact model,[23] which neglects the particular structure of the colloidal monolayer and yields an effective response of the particle ensemble to give an indentation modulus to compare with other coatings. In a more detailed analysis, a consecutive contact model is introduced to uncover the mechanics of indentation on particle arrays. Because the relevant geometrical features such as the particle radius and shell thickness are determined independently by transmission electron microscope (TEM) observations and the indentor radius R_d was specified by the manufacturer and measured by optical microscopy the only adjustable parameter, the elastic modulus of the single HSNP, can be extracted when fitting the experimental indentation force−displacement curves of HSNP arrays with the model. This model has been adopted from models of the indentation behavior of vertical arrays of straight[24,25] and coiled carbon nanotubes,[26] which have recently been studied to understand the collective behavior of nanotube forests and determine the elastic properties of a single nanotube.[24]

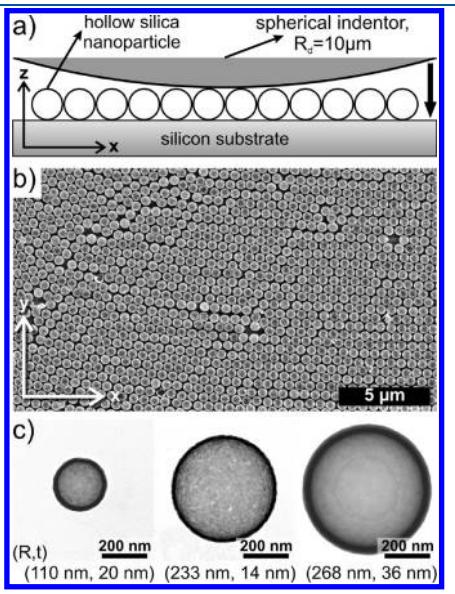

Figure 1. (a) Schematic illustration of nanoindentation on a 2D periodic monolayer of close-packed HSNPs using a spherical indentor with a tip radius of R_d = 10 μm. (b) SEM image of the particle array. (c) TEM images of individual constituent HSNPs with different midsurface radii R and shell thicknesses t.

RESULTS AND DISCUSSION

The nanoindentation on a HSNP array is schematically illustrated in Figure 1a, where a scanning electron microscope (SEM) image of a monolayer of hexagonally close-packed HSNPs on a silicon substrate is shown in Figure 1b. In this study, seven different HSNPs spanning a size ranging from about 100 to 300 nm in midsurface radius R and shell thickness t ranging from 14 to 44 nm are investigated. The standard deviation of the particle diameter and the shell thickness ranges from 1 to 4% and from 3 to 10%, respectively. TEM images of three HSNPs are shown in Figure 1c. The preparation of the HSNP films and the nanoindentation experiment are described in Sections I and II of the Supporting Information. The collective mechanical response of the HSNP films is probed via a spherical indentor with a radius of R_d = 10 μm, which is about 40−90 times larger than the radius of the constituent HSNPs.

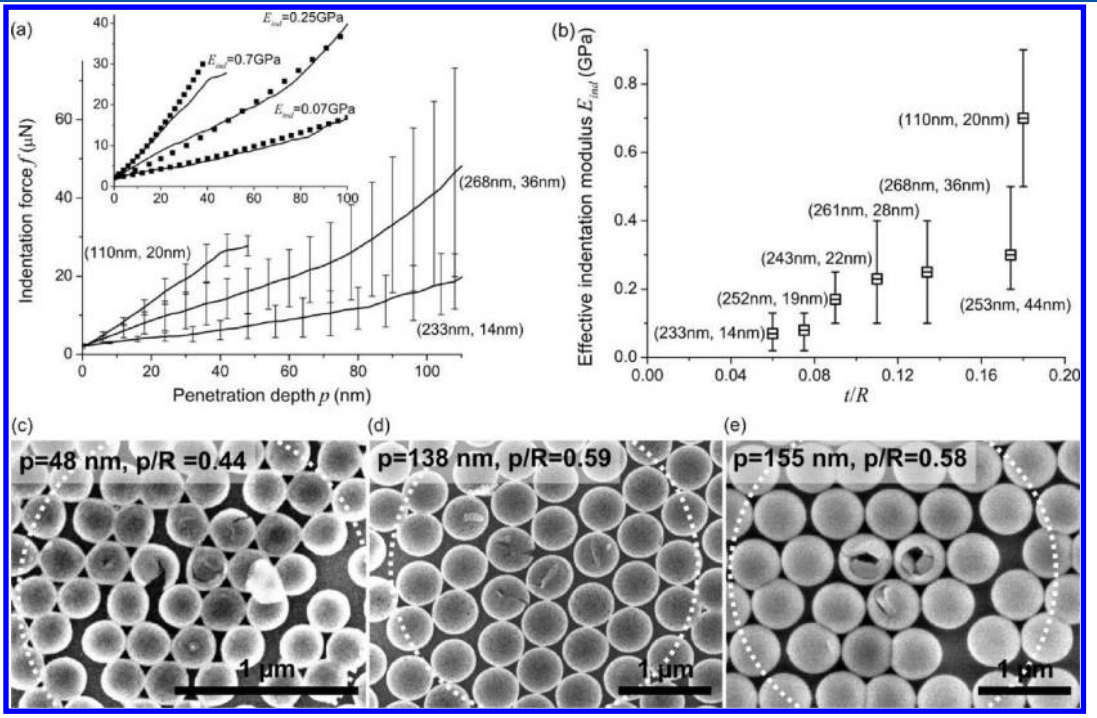

Figure 2. (a) Three representative averaged nonlinear $f-p$ curves (—) of nanoindentation on HSNP arrays with different particle geometries. The inset shows the fit of experimental curves with a Hertzian model (■). (b) Effective indentation modulus of the HSNP films plotted as a function of the constituent particles' thickness to radius ratio. (c−e) SEM image of particle arrays of (110 nm, 20 nm), (233 nm, 14 nm), and (268 nm, 36 nm) after an indent, which slightly exceeded the fitted range. The dotted white circle indicates the theoretical area of contact of a 10 μm indentor at the specified penetration depth.

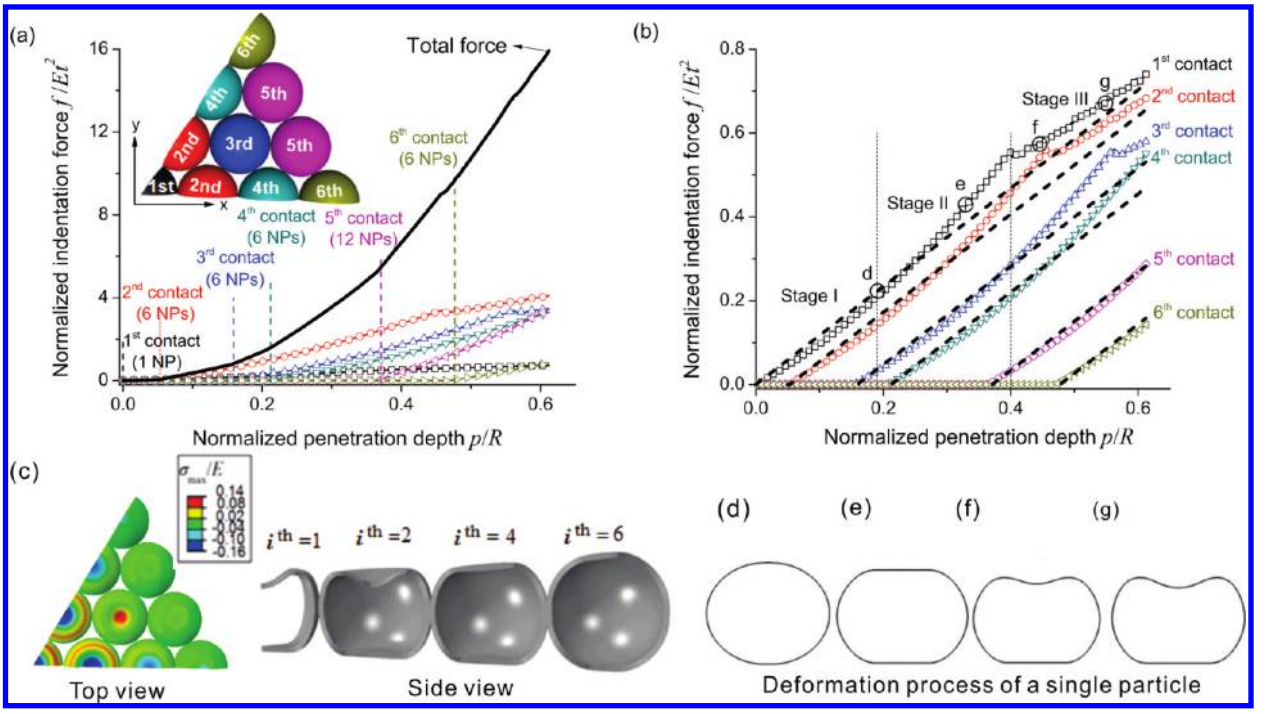

Figure 3. (a) Normalized $f-p$ curve for a monolayer of close-packed HSNPs with $t = 22$ nm, $R = 243$ nm ($t/R = 0.09$), and $E = 5$ GPa computed using finite element simulations. The total force is the superposition of the indentation forces from six successive contacts. The inset shows one-sixth of the whole structure with the particle contact sequence. (b) $f-p$ curves of individual HSNPs in each successive contact from FEM simulation (curves with symbol) and theory (eq 2, straight black dashed lines). (c) Top-view contour of the maximum principal stress σ_{max} normalized to E at $p/R = 0.6$ (left) and the side view of the deformed configuration (right). (d−g) Cross sections through four representative deformed conformations at various indentation depths of a single particle marked in b.

Effective Indentation Modulus of HSNP Films. Figure 2a shows three representative averaged experimental indentation force−penetration depth curves ($f-p$ curves) for HSNP arrays with their constituent radius and shell thickness pairs (R, t): (110 nm, 20 nm), (233 nm, 14 nm), and (268 nm, 36 nm). TEM images of these particles are given in Figure 1c. Multiple (six to nine) nanoindentation tests were conducted at different locations for each HSNP array; the averaged indentation $f-p$ curves are shown in Figure 2a. For reasons of clarity, we show only three averaged curves out of the seven particles under investigation (Figure S1, Supporting Information). The spread in the experimental data is attributed to several factors that lie in the particle and film preparation and also in the indentation experiment. Whereas the geometry of the HSNPs is well-defined and narrowly distributed, the porosity of the shell is less controllable because of its Stoeber condensation process.[27] In particular, very thin shells (~15 nm) feature rough surfaces composed of silica nanoparticles (potential failure-inducing defects) that become smoother and more homogeneous for thicker shells. The colloidal monolayer assembly process features highly ordered arrays that show line and point defects (Figure 1b). Such defects change the environment contacted by the indentor tip and thereby the resistive force. The tip geometry can also be altered throughout the course of an experiment by the unavoidable adhesion of cracked spheres to the indentor. Finally, we applied a preload (2 μN) to the tip to contact the HSNP array to determine the starting point, which therefore varied slightly from spot to spot. Despite these experimental issues, all $f-p$ curves feature the same trend of a nonlinearly increasing force as the penetration deepens. We focus on the collective elastic deformation of NP arrays that occurs prior to any fracture event. For spherical nanoindenation on an elastic, isotropic, and homogeneous film, the relationship between the indentation force f and penetration depth p is given by the classical Hertzian contact model[23]

$$f = \frac{4E_{ind}}{3(1-\nu^2)} R_d^{1/2} p^{3/2} \quad (1)$$

where E_{ind} is considered to be the effective elastic indentation modulus of the array. In this case, the monolayer of the HSNP array is approximated as a homogeneous film that reflects the collective stiffness of the HSNP film. ν is the Poisson ratio of the film and is assumed to be 0.17, a value that has been reported for porous silica monoliths prepared similarly to the silica shell in this case.[28] By fitting the averaged experimental $f-p$ curves with eq 1 as shown in the inset of Figure 2a, the effective indentation modulus E_{ind} of the HSNP films can be extracted. As mentioned earlier, a preload of 2 μN was applied to the film prior to the indentation experiment, which correspondingly indented the particle film. In the fit, this preload was accounted for by offsetting eq 1 such that $f_{(0)} = 2$ μN. Because of the simplifications of the Hertzian model, the extracted E modulus is not taken to be an intrinsic property. Whereas the constituting material $-SiO_2-$ remains fairly constant among the different samples, the geometry and density change significantly. Therefore, one should rather consider this modulus to be a kind of mechanical stiffness of the film. Indeed, when plotting E_{ind} versus its actual constituting geometry (aspect ratio t/R), one finds an unambiguous dependence (Figure 2b). E_{ind} varies systematically from 60 to 700 MPa for the seven types of HSNPs under investigation, which demonstrates the great influence of individual particle geometry and silica shell microstructure on the overall stiffness of the HSNP film. The extracted indentation modulus is in the range of a solid polymeric material and higher than the value for polymer

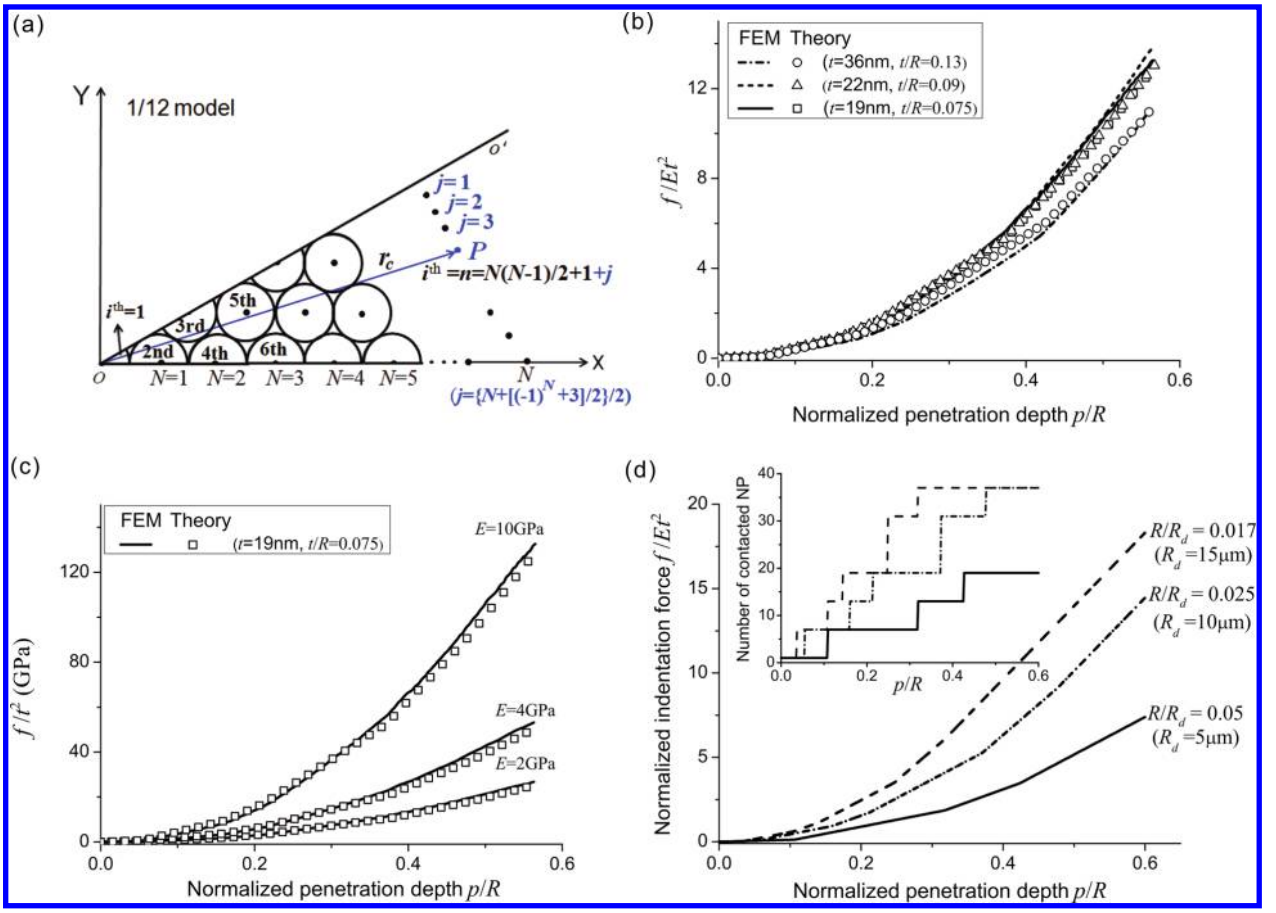

Figure 4. (a) Top view of the $^{1}/_{12}$ symmetric model with contact sequence *i*. (b, c) Comparison between FEM and the theoretical model for HSNP with different $^{t}/_{R}$ values but the same E = 5 GPa as well as for HSNPs with different E values but the same $^{t}/_{R}$ value ($^{t}/_{R}$ = 0.075). (d) Theoretically predicted effects of the indentor radius on the $f-p$ curve for particles (243 nm, 22 nm) with the indentor radius R_d ranging from 5 to 15 μm. At the same normalized indentation depth $^{p}/_{R}$, different numbers of total particles are contacted, leading to an increase in the loading force with increased indentor radius.

foams.[29] The SEM images in Figure 2c−e show that even for indents of up to $^{p}/_{R} \approx 0.6$ only a few particles underwent permanent deformation and cracking. The majority of the particles within the dotted white circle, which indicates the total area contacted by a 10 μm radius indentor at the specified penetration depth, remains unchanged. Therefore, the majority of the particles underwent only elastic deformation, which justifies the fitted range of the experimental results.

There are several key questions regarding the indentation behavior: what are the mechanisms underlying the highly nonlinear $f-p$ curves of HSNP arrays under nanoindentation? How can the relationship between the effective film indentation modulus and its constituent HSNP geometry and material properties be quantified? What are the implications for guiding the design of HSNP films with high performance?

Deformation Mechanism of Indentation on HSNP Arrays. To reveal the underlying mechanics and provide more detailed insight into the deformation mechanisms of indentation on HSNP arrays, the indentation process is modeled using the finite element method (FEM), as specified in Section II of the Supporting Information and then is analytically formulated using a consecutive particle contact model.

Owing to the symmetry of the hexagonally close-packed array, a simplified finite element model is built with a $^{1}/_{12}$ monolayer array with symmetric boundary conditions (a $^{1}/_{6}$ model is shown for better visualization in the inset of Figure 3a). Figure 3a shows the simulated, normalized $f-p$ curve with dimensionless force $\overline{f} = f/Et^2$ and penetration depth $\overline{p} = {}^{p}/_{R}$ for the case of an HSNP film with a constituent particle size (t = 22 nm, R = 243 nm, and $^{t}/_{R}$ = 0.09) and a Young's modulus of the particle shell of E = 5 GPa. This particular value of the modulus E was chosen on the basis of the experimental findings, which will be discussed later. The normalization factors, Et^2 and R, are chosen on the basis of the analytical model, which will be introduced below.

During the penetration, the HSNPs consecutively contact the indentor with the contact sequence shown in the inset of Figure 3a. The total indentation force (the black solid line) is decomposed into six successive sets of interactions (labeled with open symbols) between the indentor and particles, where multiple contacts occur simultaneously after the first contact. The increasing number of HSNPs in contact with increasing penetration depth results in the highly nonlinear behavior of the $f-p$ curve. The $f-p$ curves of individual HSNP during each consecutive contact can be extracted as shown in Figure 3b, where the force increases nonlinearly with penetration depth.

When the indentor successively encounters the HSNPs, each particle deforms in a three-stage process. Figure 3c shows the top and side views of the deformed particle array at $^{p}/_{R}$ = 0.6.

In the FEM simulation, the bottoms of the particles are firmly fixed to the substrate. Such a constraint prevents the formation of dimples on the bottom and breaks the symmetry of deformation. This also resembles the experimental situation in which the particles are fixed to the substrate by the combustion of the sacrificial core after assembly on the wafer. The strong contact between the spheres and substrate can be inferred from Figure S4 (Supporting Information), where small pieces of the bottom center parts of the silica shells reside on a hexagonal lattice even after a full indent. The structural deformation occurring on the particle's top is similar to the deformation during a planar plate compression because of the relatively larger indentor radius ($R_d/R \approx 40-90$).[30,31] The three-stage deformation process of a single particle with increasing penetration depth is shown in Figure 3d−g. Stage I is the small deformation regime with a penetration depth on the order of the HSNP's shell thickness (Figure 3d), where the force grows linearly with penetration depth as seen in the extracted $f-p$ curves of individual HSNPs in Figure 3b. This initial contact loading can be reasonably approximated as a point load, where the particle deflection p can be expressed in terms of the indentation force f and particle material properties:[32,33]

$$p = \frac{\sqrt{3(1-\nu^2)}fR}{2Et^2} - \frac{12(1+\nu)^2 f}{\pi^2 ER\sqrt{3(1-\nu^2)}} \approx \frac{\sqrt{3(1-\nu^2)}fR}{2Et^2} \tag{2}$$

The second term in eq 2 is the displacement caused by the interactions with six surrounding particles, the value of which is less than 1% of the first term for $t/R < 0.1$ and thus can be neglected. Stage II is a transition from stage I (i.e., point contact) to stage III (i.e., circular ring contact), where the particle becomes flattened to form a circular disk contact (Figure 3e, and the indentation force starts to deviate from the point model as shown in Figure 3b). With further increases in the penetration depth, local buckling occurs, which is characterized by a sharp reduction in the slope of the individual particle $f-p$ curve. The critical buckling indentation force f_{cr} scales as $f_{cr} \approx Et^3/R$ (Figure S2), which agrees with the scaling law in Pogorelov.[34] From Figure 3f, it can be seen that the contact region bends inward to form a dimple, which leads to the transition of the contact condition from a circular disk contact to a ring contact. The stress is highly concentrated in the concentric striped ring area as observed from the maximum in-plane principal stress contour in Figure 3c. This stress promotes circumferential cracking for the case of a brittle material such as the silica material when reaching a critical stress level. Circumferential cracking has indeed been observed in our samples for penetration depths larger than the range under consideration here (Figures 2e and 5d). The deformed shell conformation shows that the contact ring radius enlarges and is accompanied by the deepening of the dimple (Figure 3g).

On the basis of the deformation mechanics of a single HSNP, the total indentation force produced by the array can be predicted using a model that captures a consecutive set of elastic indentor−particle contacts. We note that simulations showed that the relative location of the indentor positioned over a particle array had little effect on the $f-p$ curve (Figure S3 in the Supporting Information). Hence, in what follows, the reduced symmetry model shown in Figure 4a, $^1/_{12}$ of a whole hexagonally close-packed monolayer, is used. The superposition of the penetration force f_i from each particle i gives rise to the total indentation force f

$$f = \sum_{i=1}^{n} \alpha_i f_i, \alpha_i = \begin{cases} 0 \text{ when } p \le p_i \\ 1 \text{ when } p > p_i \end{cases} \tag{3}$$

where α_i is equal to 1 when the indentor encounters the ith HSNP at a certain penetration depth p_i; otherwise, $\alpha_i = 0$. p_i is the displacement along the Z axis at which the indentor encounters the ith HSNP; n is the total number of particles in contact. For a small deformation ($p \le 2t$), from eq 2 f_i can be expressed as

$$f_i \approx k(p - p_i) \text{ with } k = \frac{2Et^2}{R[3(1-\nu^2]^{1/2}} \tag{4}$$

where k is defined as the stiffness of a single particle and coefficient 2 is for a whole spherical shell. Despite the small deformation assumption of eq 4, a linear relationship between f_i and p is expected for deformations up to a few times the shell thickness,[35] which is confirmed by the linear force deformation as shown in Figure 3b. For single spheres with an elastic shell, this behavior has been rationalized by the change in contact area from point contact to ring contact.[35] The encounter displacement p_i can be geometrically determined when the array is centrally indented. Given any indentation depth p with $p/R_d \ll 1$, for the ith particle P in contact as shown in Figure 4a, p_i can be expressed as

$$p_i(N,j) = \frac{(R+\frac{t}{2})^2}{2R_d}\left\{3N^2 + \left[\frac{(-1)^{N+j}-1}{2} + j\right]^2\right\}$$

$$\text{with } N = \text{int}\left|\left[\frac{2R_d}{3(R+\frac{t}{2})^2}p\right]^{1/2}\right| \tag{5}$$

where integer N is the number of circumferentially contacted annuluses away from the center and j denotes the contact sequence within the Nth annulus. The integer N is governed by the radius of the indentor and particle as well as the penetration depth p as demonstrated in eq 5. The total number of contacted particles n is determined by N and j with $n = N(N-1)/2 + 1 + j$. For a small deformation, by substituting eqs 4 and 5 into eq 3, the total indentation force f as a function of the penetration depth p is known. As an example, for the system studied in Figure 4a, at $p = 0.36R$, the indentor will contact a total of 19 particles ($N = 2$) and f can be given by

$$f = \sum_{i=1}^{n=19} k\alpha_i(p - p_i) = kp + 6k\alpha_1\left[\frac{p - 2(R+\frac{t}{2})^2}{R_d}\right] + 6k\alpha_2\left[\frac{p - 6(R+\frac{t}{2})^2}{R_d}\right] + 6k\alpha_3\left[\frac{p - 8(R+\frac{t}{2})^2}{R_d}\right] \tag{6}$$

where the terms associated with the indentor radius R_d are the encounter displacements p_i at each consecutive contact. Equation 6 demonstrates that the total indentation force f is not only proportional to the stiffness of single particles k but also associated with the total number of contacted particles n, which is determined

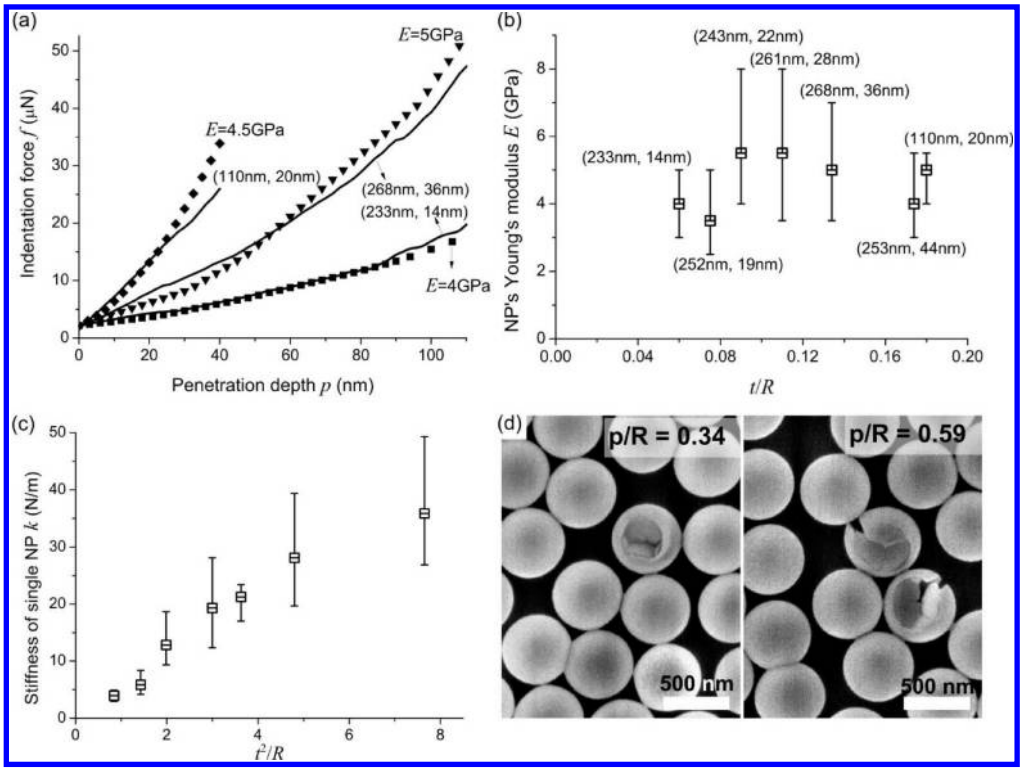

Figure 5. (a) Theoretical fitting of the averaged experimental $f-p$ curves (—) using the consecutive contact model (solid symbols). (b) Fitted Young's modulus of the silica shell of individual HSNPs. (c) The stiffness of individual particles scales with t^2/R. (d) Morphology of the (261 nm, 28 nm) particles after indentation of up to $^p/_R = 0.34$ and 0.59.

by the ratio $R_d/(R + {}^t/_2)^2$ as shown in eq 5. Normalizing eq 6 with $\bar{f} = f/Et^2$ and $\bar{p} = {}^p/_R$ shows that only the ratio R/R_d governs the onset of the nonlinearity of the normalized $f-p$ curve. For an extreme case when R_d is increased to an infinite value, the total indentation force f_{inf} will be approximated by nkp, which would be the case for a flat punch indenting a finite area with n particles.

Even though eq 4 applies only to a single spherical capsule with thin shells under small deformations, Figure 4b shows that by assuming a linear response of individual particles, the total reaction force of a monolayer of particles in eq 5 still provides good agreement with the FEM simulation with different $^t/_R$ ($^t/_R < 0.13$) values. The deviation between theory and FEM becomes larger when the particles have a relatively thicker shell. However, the thin-shell model still captures the trend for thicker shells with $^t/_R = 0.13$ as shown in Figure 4b. The good agreement is attributed to two effects, which can be seen from the $f-p$ curves of individual NPs as shown in Figure 3b. First, despite the slight deviation from the theoretical linear line (black dashed line) around the onset of buckling, the simulation curves fall back close to the line during postbuckling. As outlined above, this phenomenon has been attributed to the transition from a point contact to a ring contact upon buckling by Elsner et al.[35] Second, even at a large indentation depth (e.g., $^p/_R \approx 0.6$ in Figure 3b), a majority of the NPs are deforming in or very near the linear stage, which means that the resulting total resistance force is mainly attributed to the large number of contacts in the linear regime. Experimentally, this has been confirmed by the observation of the center portions of Figures 2c,d and 5d, where only a few particles underwent permanent deformation.

From the proposed theoretical model, the effect of the indentor radius R_d on the normalized $f-p$ curve of particle arrays can also be predicted as shown in Figure 4d. It shows that a small R/R_d ratio leads to an earlier onset of nonlinearity and a higher normalized indentation force. The reason is attributed to the different total number of particles in contact at the same normalized indentation depth $^p/_R$ as shown in the inset of Figure 4d, which is governed by R/R_d. Such behavior is also well known in the macroscopic world, for instance, from a fakir resting on a bed of nails. Understanding the influence of the R/R_d ratio on the total force is important for appropriate material design for applications such as projectiles as opposed to blast protection.

Model Applications I: Extracting the Elastic Modulus of an NP from the Indentation on NP Arrays. The mechanisms underlying the indentation on NP arrays can provide useful insights into the nature of the elastic modulus of the shell of single HSNPs as well as the connection between the effective behavior of the HSNP films and their constituent HSNPs.

Figure 5a shows the model-data fitting for the averaged experimental $f-p$ curves for three samples (110 nm, 20 nm), (233 nm, 14 nm), and (268 nm, 36 nm) (in the case of the Hertzian model, the preload is accounted for by offsetting the penetration depth). The Young's modulus of the silica shell extracted from this data is found to range from 3.5 to 8 GPa and does not show a geometry dependency within the range of error. This modulus is expected to be an intrinsic modulus and a pure material property because all geometric contributions have been taken into account. This is in contrast to E_{ind} from the Hertzian model, which explains the large difference between the two. Furthermore, the intrinsic E modulus of our amorphous silica is 10−20 times lower than that of bulk fused silica (about 72 GPa),[36] which implies a high shell porosity in our system.[37] The modulus of the silica shell of our nanoparticles is also lower than that of the single hollow silica

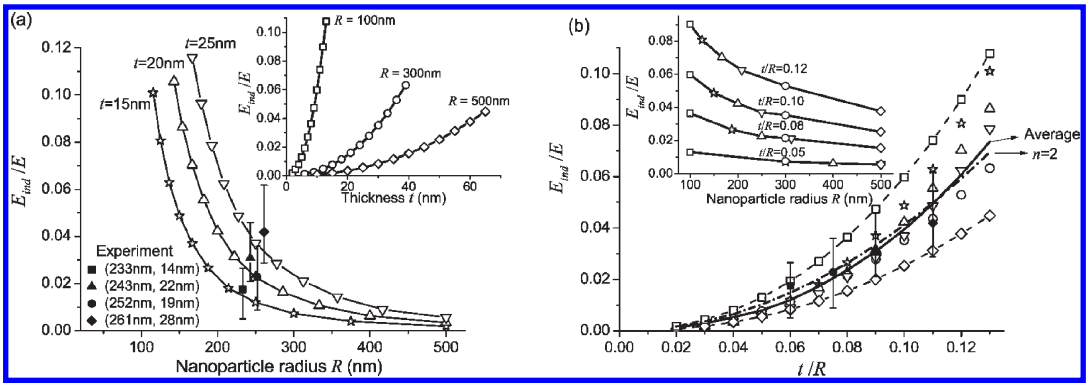

Figure 6. (a) Effect of particle radius R on the normalized effective indentation modulus of HSNP films E_{ind}/E when the particle shell thickness t is kept constant. The solid symbols are the experiment data. The inset shows E_{ind}/E versus particle thickness t when R is fixed by (b) the scaling law between E_{ind}/E and $^{t}/_{R}$ for particles with different sizes and shell thicknesses; the inset shows E_{ind}/E vs R for particles with the same $^{t}/_{R}$ value.

spheres (E = 18 ± 6 GPa) as reported by Zhang et al.,[17] which was obtained using AFM. The variation in silica porosity could also be the reason for this difference. The stiffness of a single HSNP is also extracted using eq 4 and is found to increase linearly with t^2/R and varies from 4 to 50 N/m for the particles in this study. In analogy to the Hertzian model fitting (Figure 2), the experimental results are only marginally influenced by plastically deformed hollow spheres for penetration depths of up to $^{p}/_{R} \approx 0.6$. The reason for this is the small number of cracked spheres (for example, one sphere for $^{p}/_{R}$ = 0.34 and two spheres for $^{p}/_{R}$ = 0.59, Figure 5d) and the comparatively large number of elastically loaded spheres at high deformations.

Model Applications II: Extracting the Effective Film Modulus from the Indentation Model. So far, the experimental indentation force−penetration depth curves are interpreted by two methods: one is the Hertzian model (eq 1) under the assumption of a homogeneous film, which is used for the extraction of an effective film modulus E_{ind}; the other is the consecutive contact model (eq 6), which reveals the mechanics underlying the indentation on a monolayer of nanoparticle arrays. It is straightforward to combine these two methods to obtain a predictive tool linking the effective HSNP film behavior to its constituent nanoparticles. In the following text, the focus will be placed on HSNPs with relatively thin shells ($^{t}/_{R} < 0.13$) and on small penetration depths ($\bar{p} < 0.4$). For thicker shells, the consecutive contact model will underestimate the Young's modulus of the particle material. Equating eq 1 with eq 6 gives

$$E_{ind}R_d^{1/2}\bar{p}^{3/2} = \frac{E\sqrt{3(1-\nu^2)}}{2}\frac{t^2}{R^{3/2}}\sum_{i=1}^{n}\alpha_i\left(\bar{p}-\frac{p_i(R,R_d,t)}{R}\right) \quad (7)$$

where p_i is a function of indentor radius R_d, particle radius R, and particle shell thickness t as shown in eq 5. Equation 7 demonstrates that E_{ind} is directly proportional to the elastic modulus E of the particle shell material. Because the right part of eq 7 is a discrete function depending on the value of p_i, the fitting of E_{ind} in eq 7 must be solved numerically.

To be consistent with the experiments, the radius of the nanoparticles under investigation ranges from 100 to 500 nm and the thickness to radius ratio $^{t}/_{R}$ varies from 0.02 to 0.13, where particles with the same shell thickness (t = 15 nm, 20 nm, and 25 nm) and particles with the same radius (R = 100 nm, 300 nm, and 500 nm) are systematically explored numerically as $^{t}/_{R}$ is adjusted. Figure 6a shows numerical solutions of the normalized effective indentation modulus E_{ind}/E as a function of the particle radius and shell thickness. The results show that E_{ind} varies between 0.1 and 10% of the constituent particle's material modulus for particles with $^{t}/_{R}$ varying from 0.02 to 0.13. Normalization with respect to E removes the influence of the actual material property of the shell of the hollow sphere. Thus, only geometric differences will cause differences among various samples. E_{ind}/E increases with shell thickness t at fixed R and increases with decreasing particle radius R at fixed t as shown in Figure 6a, which is a consequence of the constituting spheres' stiffness. The inset of Figure 6b shows the variation of E_{ind}/E for particle radii from 100 to 500 nm at different $^{t}/_{R}$ values and hence film densities ρ_{film} ($^{t}/_{R}$ = 0.05, 0.08, 1.0, and 1.2) as seen in eq 8

$$\frac{\rho_{film}}{\rho_{bulk}} = 0.52\left[1-\left(\frac{1-\frac{0.5t}{R}}{1+\frac{0.5t}{R}}\right)^3\right] \quad (8)$$

where ρ_{bulk} is the density of fused bulk silica. Equation 8 demonstrates that the film density is associated only with the relative shell thickness $^{t}/_{R}$ of the constituent particle. For thin shells with relatively small $^{t}/_{R}$ values (e.g., for particles with $^{t}/_{R} < 0.06$), the curve of E_{ind}/E versus R is close to a horizontal line as shown in the inset of Figure 6b, which means that for low-density films the actual particle size has a relatively minor influence on the effective indentation modulus of the film. This indicates that for films with the same small $^{t}/_{R}$ of constituent particles, films composed of large particles and thus thick shells offer a very similar stiffness to that of those composed of smaller particles with thinner shells. However, this situation changes for films with higher densities. As can be seen from the inset in Figure 6b, with the increase in $^{t}/_{R}$, the value of E_{ind}/E decreases rapidly with the increasing particle size (R), which means that films composed of smaller particles give a much higher stiffness than those composed of large particles. In this case, it is preferable to use smaller particles over larger ones. Despite the effect of particle size or shell thickness on E_{ind}, Figure 6b shows that generally E_{ind}/E increases nonlinearly with $^{t}/_{R}$. The data fit of E_{ind}/E shows a scaling power law with $E_{ind}/E = A(^{t}/_{R})^{n}$ for particles with different $^{t}/_{R}$ values, where A demonstrates the geometric effect of the number of particles in contact, which is related to the particle radius. Exponent n = 2.3 ± 0.2 shows the influence of the relative shell thickness on the effective modulus of an individual hollow particle.

The solid line in Figure 6b is the average value of the calculated particles, which shows a scaling power with $A_{av} \approx 8$. The dashed lines in Figure 6b represent the upper and lower values for the particles of radius R = 100 and 500 nm with A_{upp} = 12 and A_{low} = 5, respectively. The relatively smaller particle radius leads to an increasing number of particles in contact, which gives rise to a higher value of A. A theoretical estimation of the value of exponent n can be obtained from a scaling relationship based on an approximate modified Hertzian contact model, where the indented solid spheres are replaced with hollow ones. For a single hollow sphere, in terms of eq 2, the effective indentation modulus is found to scale as $E_{ind} \propto E({}^{t}/_{R})^{2}$ using an equivalent strain to scale of $\varepsilon \approx {}^{p}/_{R}$ and an equivalent stress to scale of $\sigma \approx f/\pi R^{2}$. This rough estimate gives an exponent of 2, which agrees with the numerical solutions shown by a dashed−dotted curve (Figure 6b). From Figures 2b and 5b, E_{ind}/E from the experimental data (labeled with solid symbols) can be deduced, which shows good agreement with the numerical solutions (Figure 6a). In addition, the experimental data is consistent with the power law trend when ${}^{t}/_{R} \leq 0.13$ as shown in Figure 6b. From these considerations, some useful insights into the design of a nanoparticle film with a relatively high stiffness can be obtained: to guarantee a stiffer film, constituent particles with a relatively thicker shell (increasing ${}^{t}/_{R}$) is the first choice; under the precondition of a constant film density, particles with a smaller size are preferred to give a relatively higher effective indentation modulus.

CONCLUSIONS

The collective nonlinear behavior of an ordered monolayer of hollow silica nanoparticles under nanoindentation was investigated through numerical, theoretical, and experimental studies. By assuming the HSNP array to be a continuous and homogeneous film, the effective indentation modulus E_{ind} was found to range between 60 and 700 MPa for constituent hollow particles with a radius of 100−300 nm and a shell thickness of 14−44 nm. Deformation mechanisms of individual hollow spheres in the HSNP array were identified using finite element simulation of the indentation process. The contacted individual particles consecutively undergo the same three stages of deformation from local bending to a flattened top to a buckled dimpled top. A consecutive contact model was established to predict the nonlinear behavior of the indentation force versus displacement curves on HSNP arrays. The superposition of the assumed linear elastic response of individual NPs showed good agreement between simulations and experiments. The model reveals that the nonlinear behavior of the indentation force−penetration depth curve is primarily attributed to contacting increasing numbers of particles as the contact area increases, which is governed by R/R_d. The consecutive contact model was applied to extract the Young's modulus of the silica shell of HSNPs from experiments on arrays, the value of which varied from 3.5 to 8 GPa in this study. By combining the Hertzian and the consecutive contact model, we established a quantitative method to tailor the effective indentation modulus E_{ind} of a HSNP film by manipulating the geometry and modulus of constituent HSNPs. A Hertzian-like contact of the hollow sphere shows the indentation modulus to scale with the particle shell modulus and geometry as $E_{ind} = EA({}^{t}/_{R})^{2}$, with coefficient A varying from about 5 to 12 for particles with radii of 100 to 500 nm. We conclude that an increase in film density will always lead to stiffer films. Under the premise of a fixed film density, we find that for a particle aspect ratio of ${}^{t}/_{R} < 0.05$ the actual particle dimensions have a minor influence on the collective performance. In the range of $0.05 < t/R < 0.13$, smaller particles with a thinner shell feature a higher effective film stiffness than for larger particles with a thicker shell of equal density.

ASSOCIATED CONTENT

Supporting Information. Details of the preparation of nanoparticle arrays and nanoindentation tests and FEM modeling. Scaling of the critical buckling force with ${}^{t}/_{R}$. Effect of the indentor location on the $f-p$ curves. SEM images showing the firm contact between spheres and substrate. This material is available free of charge via the Internet at http://pubs.acs.org.

AUTHOR INFORMATION

Corresponding Author

*E-mail: mcboyce@mit.edu.

Author Contributions

‖These authors contributed equally to this article.

ACKNOWLEDGMENT

This research was supported by the U.S. Army Research Office through the Institute for Soldier Nanotechnology under contract W911NF-07-D-0004. M.R. acknowledges support by the Alexander-von-Humboldt Foundation. We thank Alan Schwartzman for experimental support. We acknowledge the anonymous reviewers for their valuable comments and suggestions.

REFERENCES

(1) Lou, X. W.; Archer, L. A.; Yang, Z. *Adv. Mater.* **2008**, *20*, 3987.
(2) Dimitrov, A. S.; Nagayama, K. *Langmuir* **1996**, *12*, 1303.
(3) Goldenberg, L. M.; Wagner, J.; Stumpe, J.; Paulke, B. R.; Gornitz, E. *Langmuir* **2002**, *18*, 3319.
(4) van Duffel, B.; Ras, R. H. A.; de Schryver, F. C.; Schoonheydt, R. A. *J. Mater. Chem.* **2001**, *11*, 3333.
(5) Chen, Z.; Zhan, P.; Wang, Z.; Zhang, J.; Zhang, W.; Ming, N.; Chan, C. T.; Sheng, P. *Adv. Mater.* **2004**, *16*, 417.
(6) Pang, J.; Xiang, S.; Jaeckel, F.; Sun, Z.; Dunphy, D.; Brinker, C. J. *J. Am. Chem. Soc.* **2008**, *130*, 3284.
(7) Sun, Z.; Bai, F.; Wu, H.; Schmitt, S. K.; Boyce, D. M.; Fan, H. *J. Am. Chem. Soc.* **2009**, *131*, 13594.
(8) Kowalczyk, B.; Apodaca, M. M.; Nakanishi, H.; Smoukov, S. K.; Grzybowski, B. A. *Small* **2009**, *17*, 1970.
(9) Hoogenboom, J. P.; Retif, C.; de Bres, E.; van de Boer, M.; van Langen-Suurling, A. K.; Romijn, J.; van Blaaderen, A. *Nano Lett.* **2004**, *4*, 205.
(10) Son, S. J.; Bai, X.; Lee, S. B. *Drug. Discovery Today* **2007**, *12*, 650.
(11) Liu, Y.; Miyoshi, H.; Nakamura, M. *Int. J. Cancer* **2007**, *120*, 2527.
(12) Astruc, D. *Nanoparticles and Catalysis.*: Wiley-VCH: Weinheim, Germany, 2007.
(13) Colvin, V. L. *MRS Bull.* **2001**, *26*, 637.
(14) Shipway, A. N.; Katz, E.; Willner, I. *ChemPhysChem* **2000**, *1*, 18.
(15) Sun, S. H.; Murray, C. B.; Weller, D.; Folks, L.; Moser, A. *Science* **2000**, *287*, 1789.
(16) Fery, A.; Weinkamer, R. *Polymer* **2007**, *48*, 7221.
(17) Zhang, L.; D'Acunzi, M.; Kappl, M.; Auernhammer, G. K.; Vollmer, D.; Kats, C. M.; Blaaderen, A. *Langmuir* **2009**, *25*, 2711.
(18) Zhang, L.; D'Acunzi, M.; Kappl, M.; Imhof, A.; van Blaaderen, A.; Butt, H.-J.; Graf, R.; Vollmer, D. *Phys. Chem. Chem. Phys.* **2010**, *12*, 15392.

(19) Shan, Z. W.; Adesso, G.; Cabot, A.; Sherburne, M. P.; Syed Asif, S. A.; Warren, O. L.; Chrzan, D. C.; Minor, A. M.; Alivisatos, A. P. *Nat. Mater.* **2008**, *7*, 947.
(20) Sanders, W. S.; Gibson, L. J. *Mater. Sci. Eng., A* **2003**, *347*, 70.
(21) Mueggenburg, K.; Lin, X.-M.; Goldsmith, R. H.; Jaeger, H. M. *Nat. Mater.* **2007**, *6*, 656.
(22) Evans, A. G.; Hutchinson, J. W.; Ashby, M. F. *Prog. Mater. Sci* **1999**, *43*, 171.
(23) Johnson, K. L. *Contact Mechanics*; Cambridge University Press: Cambridge, U.K., 1985.
(24) Wang, L.; Ortiz, C.; Boyce, M. C. *J. Eng. Mater. Technol.* **2011**, *133*, 011014.
(25) Qi, H. J.; Teo, K. B. K.; Lau, K. K. S.; Boyce, M. C.; Milne, W. I.; Robertson, J.; Gleason, K. K. *J. Mech. Phys. Solids* **2003**, *51*, 2213.
(26) Coluci, V. R.; Fonseca, A. F.; Galvao, D. S.; Daraio, C. *Phys. Rev. Lett.* **2008**, *100*, 086807.
(27) Stober, W.; Fink, A.; Bohn, E. *J. Colloid Interface Sci.* **1968**, *26*, 62.
(28) Adachi, T.; Sakka, S. *J. Mater. Sci.* **1990**, *25*, 4732.
(29) Ashby, M. F. *Materials Selection in Mechanical Design*, 2nd ed.; Butterworth-Heinemann: Boston, 1999.
(30) Kitching, R.; Houlston, R.; Johnson, W. *Int. J. Mech. Sci.* **1975**, *17*, 693.
(31) Glynos, E.; Koutsos, V.; McDicken, W. N.; Moran, C. M.; Pye, S. D.; Ross, J. A.; Sboros, V. *Langmuir* **2009**, *25*, 7514.
(32) Reissner, E. *J. Math. Phys.* **1949**, *25*, 279.
(33) Koiter, W. T. In *Progress in Applied Mechanics (The Prager Anniversary Volume)*; Drucker, D. C., Ed.; Macmillan: New York, 1963; pp 155−169.
(34) Pogorelov, A. V. *Bendings of Surfaces and Stability of Shells*; American Mathematical Society: Providence, RI, 1988.
(35) Elsner, N.; Dubreuil, F.; Weinkamer, R.; Wasicek, M.; Fischer, F. D.; Fery, A. *Prog. Colloid Polym. Sci.* **2006**, *132*, 117.
(36) Bhushan, B. *Handbook of Nanotechnology*; Springer: Berlin, 2004.
(37) Mori, T.; Tanaka, K. *Acta Metall.* **1973**, *21*, 571.